Local dilation and compaction of granular materials induced by plate drag

Murino Kobayakawa,[1] Shinichiro Miyai,[1,2,3] Takuya Tsuji,[1,2,*] and Toshitsugu Tanaka[1,2]
[1]*Komatsu MIRAI Construction Equipment Cooperative Research Center, Osaka University, 2-1 Yamada-oka, Suita, Osaka 565-0871, Japan*
[2]*Department of Mechanical Engineering, Osaka University, 2-1 Yamada-oka, Suita, Osaka 565-0871, Japan*
[3]*Development Division, Komatsu Ltd., 1200 Manda, Hiratsuka, Kanagawa 254-8567, Japan*

(Received 19 January 2018; published 20 November 2018)

The response of granular materials to plate drag is numerically studied using a large-scale discrete element method (DEM) simulation. The effect of the initial volume fraction of the materials on the drag force acting on the plate is examined. The results show that a volume-fraction-dependent bifurcation occurs in the force; in an initially loose granular bed, the force reaches an approximately constant value as the plate advances, while in an initially dense bed, the force oscillates with a large amplitude. The force oscillation is attributed to the periodic evolution of a shear band formed only in the dense bed. The behaviors of the drag force and shear band, which depend on the initial volume fraction in the DEM simulation, are in close agreement with those obtained experimentally in previous studies [N. Gravish *et al.*, Phys. Rev. Lett. **105**, 128301 (2010); Phys. Rev. E **89**, 042202 (2014)]. Further analysis using the DEM simulation shows that the formation of the shear band is explained by the local dilation and compaction of the granular materials induced by the plate drag. Independent of the volume fraction, materials dilate in a wedge-shaped flow region that formed in front of the plate. In the loose bed, a compacted front builds up ahead of the flow region. Because the compacted front advances into a weaker undisturbed region, the flow region behind the front can constantly advance. On the other hand, in the dense bed, the materials largely dilate in a disturbed flow region formed in front of the plate. Because a denser undisturbed region is more stable compared to the flow region, the flow region is strongly confined. As a result, the shear strain is localized along a flow boundary between these regions, and the shear band develops.

DOI: 10.1103/PhysRevE.98.052907

I. INTRODUCTION

Granular materials significantly exhibit different behaviors from continuums [1–3]. Recently, forces experienced by objects moving in granular materials have been studied extensively in different configurations, such as impact [4–7], vertical penetration [8–11], and intruder drag [12–20]. Plate drag [13,15,18], which is the focus of this study, is one of these configurations, and is a simple but important example of localized forcing, because it provides an understanding of how animals, robots, and tools interact with the soil during their locomotion [21–24].

One of the most important parameters that affect the dynamic responses of granular materials subjected to external perturbations is the volume fraction ϕ of the materials. ϕ is defined as the ratio of the particle volume to the total volume occupied by the packing, and typically varies between the random loose-packing limit ($\phi = 0.55$) and the random close-packing limit ($\phi = 0.64$) for ideal monodisperse sphere packing [25]. The sensitivity of the initial volume fraction ϕ_0 on the response was observed in compression test [26–28], avalanche [29–32], vertical penetration [8,10], impact [6,7], and plate drag [13,18] scenarios.

In general, loosely packed granular materials compact under shear, while closely packed materials dilate under shear [33]. The volume fraction at which the transition from compaction to dilation occurs is called a critical fraction ϕ_c, which is a function of the friction coefficient between particles [28].

Gravish *et al.* experimentally studied the response of dry granular materials composed of spherical glass particles to plate drag as a function of ϕ_0 [13,18]. In the experiments, a vertical flat plate was translated horizontally from rest through initially homogeneous materials with different values of $\phi_0 (0.579 < \phi_0 < 0.619)$, and the drag force acting on the plate and velocity fields in the materials were measured. The results showed that a ϕ_0-dependent bifurcation occurs in the force at the critical fraction ϕ_c ($\phi_c = 0.603$), which corresponds to the onset of dilatancy; above ϕ_c, force fluctuations are periodic and increase in magnitude with ϕ_0. The velocity field measurements indicated that the stability and the spatiotemporal evolution of a shear band formed in the materials differ as a function of ϕ_0; for $\phi_0 < \phi_c$, the shear band fluctuates in space and time, and for $\phi_0 > \phi_c$, the shear band remains almost stationary. The periodic fluctuation in the force results from the formation of the stable shear band above ϕ_c, which is created and destroyed periodically during the drag. In addition, they pointed out that the formation of the stable shear bands can be explained by the process of granular shear strengthening or weakening accompanied by local compaction or dilation below or above ϕ_c. Therefore, a spatial heterogeneous distribution of volume fraction ϕ induced in the materials by the plate drag is the origin of the ϕ_0-dependent force fluctuation. However, such a distribution of ϕ has not been investigated because the local volume fraction in materials is a quantity that is not easily measurable

*tak@mech.eng.osaka-u.ac.jp

in experiments. In many experiments, only the change in the sample's bulk volume was evaluated [6,9,10,13,18,32]. Numerical studies based on the discrete element method (DEM) allow us to access the local volume fraction (e.g., volume fraction inside the shear band).

Using DEM, we previously simulated plate drag in initially dense granular materials (close to the random close packing), and we examined the size effects of particles on the drag force and the evolution of a shear band that is formed in the materials under the same ϕ_0 [34]. The results showed that for larger size of the particles relative to the intrusion depth of the plate, the force exhibits random fluctuations while for the smaller-sized particles, the force fluctuations become periodic, and the amplitude of the oscillation increases. In conclusion, the large particles cannot reproduce the periodic force fluctuations observed in the experiments by Gravish *et al.* owing to a vague, wide shear band of the large particles. This means that a large-scale simulation using a large number of small particles is necessary to numerically analyze the plate drag.

In this study, the response of granular materials to plate drag as a function of ϕ_0 is numerically investigated using a large-scale DEM simulation. First, we show the simulated behaviors of the drag force, granular flow, and shear band depending on ϕ_0 in the DEM. Then, we analyze the local volume fraction in the materials during the drag, and show the heterogeneity in the local fraction for different values of ϕ_0. Finally, we discuss the relationship between the local dilatancy and the force bifurcation.

II. CALCULATION METHOD

A. Discrete element method

To simulate the plate drag of granular materials, we used DEM [35]. The motion of all particles is determined by solving Newton's equation of motion of individual particles. The translational equation of motion of particle i is given by the following equation:

$$m_i \frac{d\boldsymbol{v}_i}{dt} = \sum_j \boldsymbol{F}_{ij} + m_i \boldsymbol{g}, \tag{1}$$

where m_i is the mass of the particle i, $\boldsymbol{v}_i$ is the velocity, t is the time, $\boldsymbol{F}_{ij}$ is the contact force acting on the particle i from another particle j, and $\boldsymbol{g}$ is the gravitational acceleration vector. The contact force $\boldsymbol{F}_{ij}$ is decomposed into normal and tangential components; the normal direction is defined as the direction of an axis connecting the center of the particles, and the tangential direction is perpendicular to the normal direction. Each component is modeled by a linear spring, a dashpot, and a frictional slider, and is expressed as

$$\boldsymbol{F}_{n,ij} = -k_n \boldsymbol{\delta}_{n,ij} - \eta_n \boldsymbol{v}_{n,ij}, \tag{2}$$

$$\boldsymbol{F}_{t,ij} = -k_t \boldsymbol{\delta}_{t,ij} - \eta_t \boldsymbol{v}_{t,ij}, \tag{3}$$

$$\boldsymbol{F}_{t,ij} = -\mu_s |\boldsymbol{F}_{n,ij}| \frac{\boldsymbol{v}_{t,ij}}{|\boldsymbol{v}_{t,ij}|} \quad (|\boldsymbol{F}_{t,ij}| > \mu_s |\boldsymbol{F}_{n,ij}|), \tag{4}$$

where the subscripts "n" and "t" represent the normal and tangential directions, respectively; k is the spring constant; η is the damping coefficient of the dashpot; and μ_s is the coefficient of the sliding friction. $\boldsymbol{\delta}_{n,ij}$ is the normal overlap between particle i and j, which is computed from their center positions $\boldsymbol{x}_i$ and $\boldsymbol{x}_j$ and their radii r_i and r_j; $\boldsymbol{\delta}_{n,ij} = [|\boldsymbol{x}_i - \boldsymbol{x}_j| - (r_i - r_j)]\boldsymbol{n}_{ij}$, where $\boldsymbol{n}_{ij} = (\boldsymbol{x}_i - \boldsymbol{x}_j)/|\boldsymbol{x}_i - \boldsymbol{x}_j|$. $\boldsymbol{v}_{ij}$ is the relative velocity between particles i and j. $\boldsymbol{v}_{ij} = \boldsymbol{v}_i - \boldsymbol{v}_j$. $\boldsymbol{\delta}_{t,ij}$ is the relative tangential displacement of the particles since the beginning of the contact. To reproduce the sliding behavior in agreement with Coulomb's friction law, when $|\boldsymbol{F}_{t,ij}|$ calculated from Eq. (3) becomes greater than $\mu_s|\boldsymbol{F}_{n,ij}|$, the value of $\boldsymbol{F}_{t,ij}$ is recalculated by Eq. (4).

The rotational equation of motion of particle i is given by the following equation:

$$I_i \frac{d\boldsymbol{\omega}_i}{dt} = \sum_j \boldsymbol{T}_{ij}, \tag{5}$$

where I_i is the moment of inertia and $\boldsymbol{\omega}_i$ is the angular velocity. $\boldsymbol{T}_{ij}$ is the torque given by

$$\boldsymbol{T}_{ij} = \boldsymbol{R}_{ij} \times (\boldsymbol{F}_{t,ij} + \boldsymbol{F}_{r,ij}), \tag{6}$$

where $\boldsymbol{R}_{ij}$ is the vector from the center of the particle i to the contact point, and $\boldsymbol{F}_{r,ij}$ is the rolling resistance. We used spherical elements in the DEM simulation because of their numerical efficiency. However, the simulation using the spherical elements cannot accurately predict the behavior of real particles with surface roughness owing to the excessive rotation of the elements. In this study, to consider the effects of the roughness of the particle surface in the DEM, the rolling resistance model proposed by Iwashita and Oda [36] was introduced. They proposed a rotational spring-dashpot-slider model for rolling resistance similar to the above model for sliding resistance. In this model, the rolling resistance is given by

$$\boldsymbol{F}_{r,ij} = -k_r \boldsymbol{\delta}_{r,ij} - \eta_r \boldsymbol{v}_{r,ij}, \tag{7}$$

$$\boldsymbol{F}_{r,ij} = -\mu_r |\boldsymbol{F}_{n,ij}| \frac{\boldsymbol{v}_{r,ij}}{|\boldsymbol{v}_{r,ij}|} \quad (|\boldsymbol{F}_{r,ij}| > \mu_r |\boldsymbol{F}_{n,ij}|), \tag{8}$$

where k_r is the stiffness of the rotational spring, η_r is the damping coefficient of the rotational dashpot, μ_r is the coefficient of the rolling friction, $\boldsymbol{\delta}_{r,ij}$ is the relative rolling displacement of the particles since the beginning of the contact, and $v_{r,ij}$ is the relative rolling velocity. Similar to the sliding friction, when $\boldsymbol{F}_{r,ij}$ calculated from Eq. (7) becomes greater than $\mu_r|\boldsymbol{F}_{n,ij}|$, the value of $\boldsymbol{F}_{r,ij}$ is recalculated with Eq. (8).

The sliding friction and the rolling resistance were also introduced to particle-plate and particle-wall contacts.

B. Calculation condition

Figure 1(a) shows an oblique view of the simulation setup (see Supplemental Material [37]). The drag was performed in a container with a length L of 540 mm, width W of 240 mm, and height H of 200 mm. The container was sufficiently large to avoid wall effects on the drag because we did not find a large difference irrespective of container size (the result will be shown later). The container was filled with randomly packed spherical particles. The random packing was prepared using a falling method, where the particles were given initial

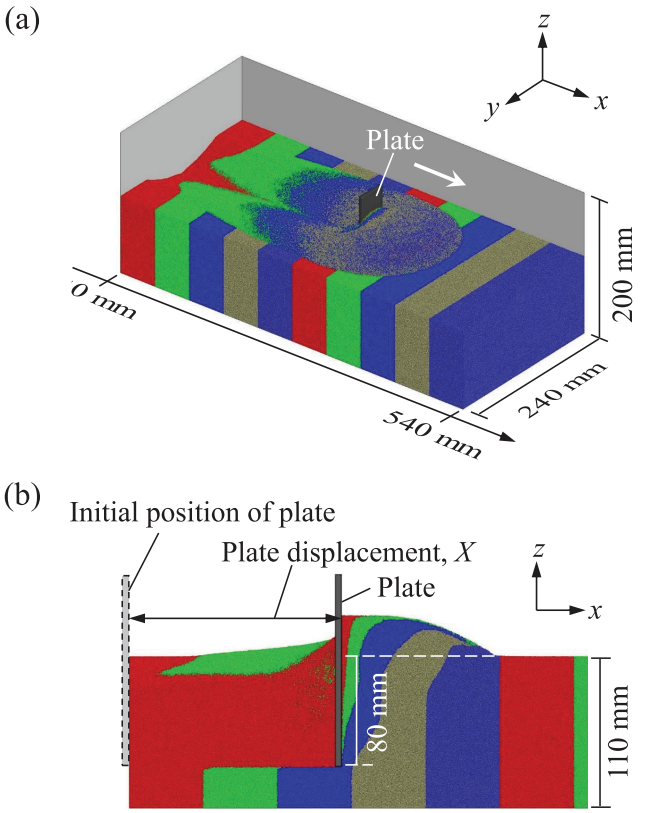

FIG. 1. Simulation setup. (a) Oblique view of the setup. The white arrow denotes the direction of plate motion. (b) Vertical cross section through the center of the plate.

random velocities and fell under gravity. The initial bulk volume fraction of the prepared bed ϕ_0 before the plate drag was controlled by varying the coefficient of sliding friction μ_{s0} and the coefficient of rolling friction μ_{r0} between particles during the packing process. After the preparation of the bed, the coefficients of the sliding and rolling friction were set to new values, i.e., μ_s and μ_r, respectively, independent of μ_{s0} and μ_{r0} [28]. Then, the beds were relaxed until they reached steady states. We measured ϕ_0 after the relaxation process ($\phi_0 = 0.586-0.638$) and started the plate drag.

A vertical plate with a width of 40 mm, height of 140 mm, and thickness of 5 mm was constantly accelerated from rest to a speed $V = 100\,\mathrm{mm/s}$ for 0.1 s (plate displacement $X = 0-5\,\mathrm{mm}$), and then translated horizontally at the constant speed through the materials. The plate depth was set to 80 mm [see Fig. 1(b)]. In this study, the plate size, depth, and speed were nearly identical to those in the experiments performed by Gravish *et al.* The calculation parameters of the DEM simulation are listed in Table I. The normal spring constant of the particles k_n was chosen as $1.0 \times 10^5\,\mathrm{N/m}$ according to preliminary computations in which k_n was varied within the range from 1.0×10^3 to $1.0 \times 10^6\,\mathrm{N/m}$. This value was chosen because values of k_n in the range from 1.0×10^5 to $1.0 \times 10^6\,\mathrm{N/m}$ do not significantly affect the drag force acting on the plate. The tangential spring constant of the particles k_t was chosen as $2.5 \times 10^4\,\mathrm{N/m}$ because k_t/k_n was assumed to be equal to Poisson's ratio of glass (0.25). The damping coefficient for the normal direction η_n can be determined

TABLE I. Calculation parameters.

Parameter	Value
Particle diameter, d_p (mm)	0.70–0.88
Normal spring constant, k_n (N/m)	1.0×10^5
Tangential spring constant, k_t (N/m)	2.5×10^4
Particle density, ρ_p (kg/m^3)	2610
Coefficient of restitution, e	0.9
Coefficient of sliding friction, μ_s	
Particle-particle	0.3
Particle-wall	0.3
Particle-plate	0.3
Coefficient of rolling friction, μ_r	0.03
Temporal increment, Δt (s)	1×10^{-6}

analytically by using the coefficient of restitution of particles e [38]:

$$\eta_n = -\frac{2\ln e}{\sqrt{\pi^2 + (\ln e)^2}}\sqrt{m_i k_n}. \tag{9}$$

In the present study, η_n was obtained using Eq. (9), and the damping coefficient for the tangential direction η_t was obtained using Eq. (10) where the coefficient of restitution e for the tangential direction was assumed to be equal to that for the normal direction.

$$\eta_t = -\frac{2\ln e}{\sqrt{\pi^2 + (\ln e)^2}}\sqrt{m_i k_t}. \tag{10}$$

The rotational spring constant k_r and damping coefficient η_r were assumed to be k_t and η_t, respectively.

The particle properties, i.e., the particle diameter, particle density, coefficient of restitution, and coefficients of friction were obtained from our preliminary experiments using commercially available glass beads. Figure 2 shows a number-based particle size distribution. The particle diameter D_p had a narrow distribution with median diameter $D_{p50} = 0.8\,\mathrm{mm}$ and uniformity coefficient $D_{p60}/D_{p10} = 1.1$. However, we did not focus on the specific values of the parameters except for the particle size because Gravish *et al.* reported that responses similar to those obtained using glass beads were also

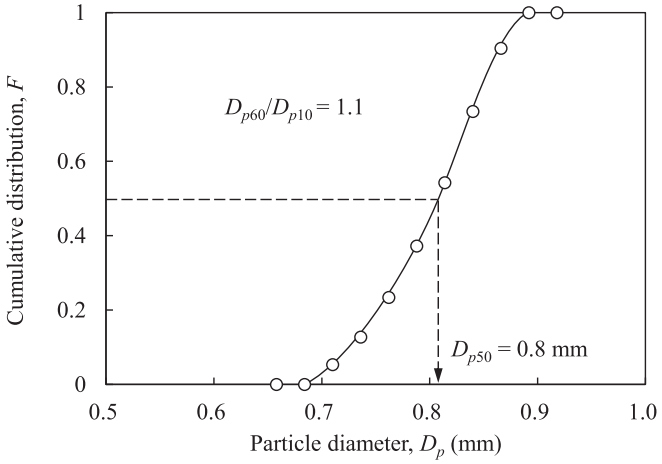

FIG. 2. Cumulative size distribution of particles.

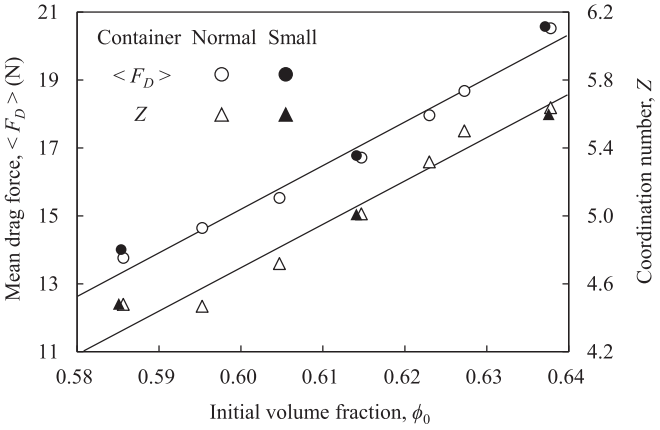

FIG. 3. Dependence of mean drag force $\langle F_D \rangle$ and coordination number Z on initial volume fraction ϕ_0 for normal-sized and small containers.

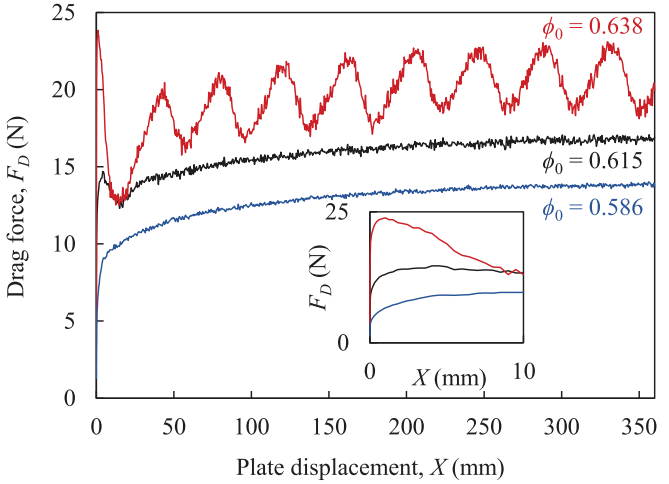

FIG. 4. Drag force F_D as a function of plate displacement X for three different values of ϕ_0. The inset shows the magnified figure of the drag force in the initial yielding process ($X = 0-10$ mm).

observed in other granular materials, including heterogeneous beach sand and poppy seeds [13,18]. The effect of the particle size on the results will be discussed later.

The DEM program code used in the study was parallelized based on the two-dimensional domain decomposition technique [39] in which the calculation domain was equally divided into subdomains along the x and y directions. Each subdomain was assigned to a processing core that computed the motion of the particles in the subdomain. Interprocessing core communication was achieved using a message passing interface (MPI) library. A parallel computer (CRAY CS400 2820XT) consisting of Intel Xeon Broadwell processors (2.1 GHz) was used. Using 1296 cores, it took 10 days to calculate the motion of 33 312 117 particles in the maximum case ($\phi_0 = 0.638$).

III. RESULTS AND DISCUSSION

A. Drag force

Figure 3 shows the mean drag force acting on the plate $\langle F_D \rangle$ and the coordination number of the initial granular bed Z as a function of ϕ_0. The mean force $\langle F_D \rangle$ is defined as the average force in the range of the plate displacement $X = 260-360$ mm, where the force reaches a steady state, and the coordination number Z is defined as the average number of contacts per particle [25]. The white plots indicate data for the normal-sized container ($L = 540$ mm, $W = 240$ mm, $H = 200$ mm), and the black plots indicate data for the smaller container ($L = 500$ mm, $W = 200$ mm, $H = 200$ mm). It can be seen that the results are similar for the normal and small containers, thus showing that these containers are sufficiently large to avoid wall effects on the drag. Hereafter, we discuss the results only for the normal container. The mean force increases approximately linearly with ϕ_0. Such a linear increase was also observed in the study by Gravish *et al.*, and they reported that it was due to an increased bed density and average coordination number [13]. From the DEM results presented in Fig. 3, it is shown that the coordination number Z increases with ϕ_0. It should be noted that the 9% increase in ϕ_0 causes a 49% increase in the force, indicating a strong dependence of the force on ϕ_0.

Figure 4 shows the drag force F_D (averaged at 200 Hz) as a function of the plate displacement X at three different values of ϕ_0. The inset is the magnified figure of the force at $X = 0-10$ mm. The forward movement of the plate causes the materials to compress, and hence for low ϕ_0, the force monotonically increases. However, for high ϕ_0, the force sharply increases until it reaches a critical value at a displacement of the order of several millimeters. Then, the force drastically decreases to $X = 10$ mm because a shear failure occurs in the materials. After this initial yielding, there is a ϕ_0-dependent force fluctuation; for low ϕ_0, the force reaches an approximately constant value as the plate advances, while for high ϕ_0, the force oscillates with a large amplitude.

The behavior of the drag force with ϕ_0 shown in this subsection is consistent with what has been obtained experimentally in previous studies [13,18].

B. Critical volume fraction

To evaluate the dependence of the compaction-dilation response of the granular bed on ϕ_0, the bulk volume fraction of the static bed after the drag ϕ_f is calculated from the resultant surface profile of the trough left behind the plate in a manner similar to that of the experiments. The change in bulk volume fraction before and after the drag $\phi_f - \phi_0$ is shown in Fig. 5, where ϕ_f is measured in three different ranges ($x = 0-100$ mm, 100–200 mm, and 200–300 mm). The positive and negative values of $\phi_f - \phi_0$ indicate the compaction and dilation of the bed, respectively. The dilation transition occurs at $\phi_c = 0.593 \pm 0.001$, as determined by the zero crossing of the best-fit line. Over the three different ranges, we observe no significant difference in the determined ϕ_c. Hereafter, we refer to the initial packing state in terms of $\phi_0 - \phi_c$.

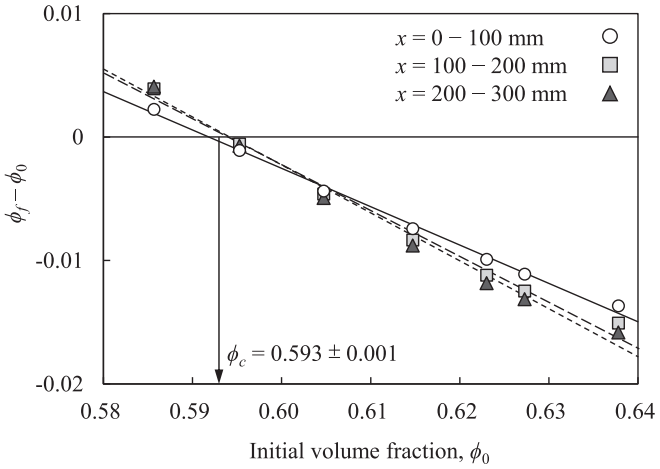

FIG. 5. Dependence of compaction-dilation response of granular beds on initial volume fraction ϕ_0. ϕ_f indicates the bulk volume fraction of the static bed after the drag, where ϕ_f is measured in three different ranges ($x = 0-100$ mm, 100–200 mm, and 200–300 mm). The positive and negative values of $\phi_f - \phi_0$ indicate the compaction and dilation of the bed, respectively. The dilation transition occurs at $\phi_c = 0.593 \pm 0.001$, as determined by the zero crossing of the best-fit line.

C. Force bifurcation

Gravish *et al.* evaluated the variation in the drag force as a function of $\phi_0 - \phi_c$ by calculating several quantities of the force, and they showed that the force exhibits two signatures of bifurcation across the dilation transition ($\phi_0 - \phi_c \approx 0$) [13,18]. We also evaluated the variation of the force in the DEM simulation by calculating the same quantities as the experiments. Figure 6(a) shows the ratio $F_{\max}/F_{D(X=10\,\mathrm{mm})}$ as a function of $\phi_0 - \phi_c$, where $F_{\max}$ is the maximum value of F_D in the initial yielding process ($X = 0-10$ mm). In the yielding process, because for $\phi_0 < \phi_c$, F_D increases monotonically with X, and thus is largest at $X = 10$ mm (see Fig. 4 inset), the ratio $F_{\max}/F_{D(X=10\,\mathrm{mm})}$ is unity. Because for $\phi_0 > \phi_c$, F_D rapidly rises to a maximum and subsequently decreases to $X = 10$ mm, the ratio exceeds unity. The result is in agreement with the experiments.

They also reported the other signature of the force bifurcation in the steady state [13]; for $\phi_0 < \phi_c$, F_D has an approximately constant value as the plate advances, while for $\phi_0 > \phi_c$, the force oscillates. Thus, the ratio of the standard deviation σ_F of the force to the mean force $\langle F_D \rangle$ sharply increases with ϕ_0 for $\phi_0 > \phi_c$. The DEM result shows that the ratio bifurcates at $\phi_0 - \phi_c \approx 0.03$, which is not in agreement with the experiments [Fig. 6(b)]; i.e., in the intermediate range of $\phi_0 - \phi_c \approx 0-0.03$, the force oscillation is not observed, even though $\phi_0 > \phi_c$. The discrepancy between the DEM and the experimental results may be attributed to the difference in the particle size used; we used particles that were about three times larger than those in the experiment (0.256 ± 0.044 mm) to reduce computational cost. In our previous DEM study, for large particles, the drag force did not oscillate even in an initially dense bed, and this was because of the vague, wide shear bands of the large particles [34].

In the following subsections, we discuss the relationships between the granular flow, shear band, and local volume fraction for the loosest packing ($\phi_0 - \phi_c = -0.007$), the intermediate packing ($\phi_0 - \phi_c = 0.022$), and the densest packing ($\phi_0 - \phi_c = 0.045$) in the DEM simulation.

D. Granular flow

Figure 7(a) shows the magnified figure of the drag force at $X = 280-360$ mm for $\phi_0 - \phi_c = -0.007$, 0.022 and 0.045 in Fig. 4. Figure 7(b) shows velocity fields in the vertical cross section through the center of the plate at $X = 311$ mm, corresponding to point A in Fig. 7(a). The color of the vectors in Fig. 7(b) represents the magnitude of the particle velocity $|\boldsymbol{v}_i|$ normalized by the plate speed V. Independent of ϕ_0, flowing particles are confined to a wedge-shaped region in front of the plate, in which the particles move forward and

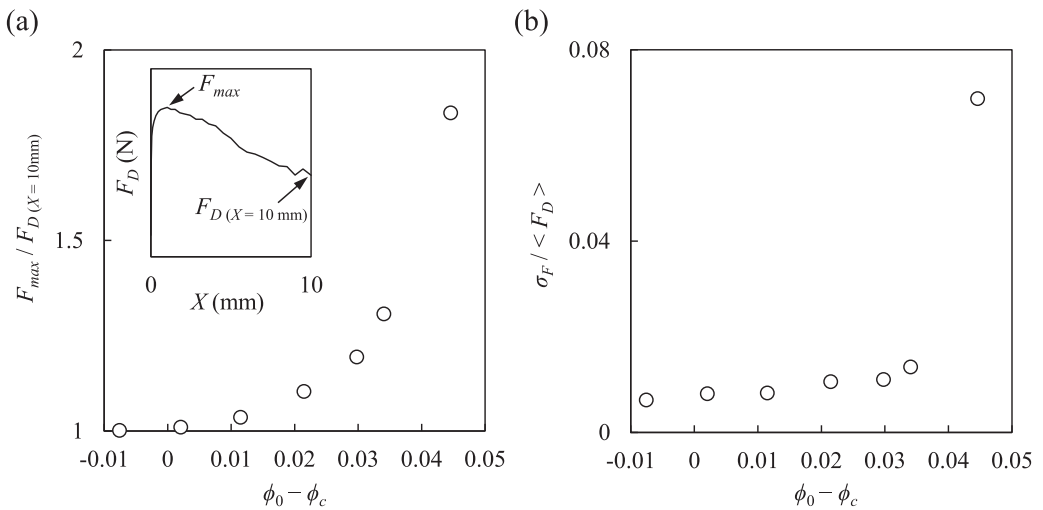

FIG. 6. Signatures of force bifurcation. (a) $F_{\max}/F_{D(X=10\,\mathrm{mm})}$ as a function of $\phi_0 - \phi_c$, where $F_{\max}$ is the maximum value of F_D in the initial yielding process ($X = 0$–10 mm). (b) $\sigma_F/\langle F_D \rangle$ as a function of $\phi_0 - \phi_c$, where σ_F is the standard deviation of F_D in the steady state ($X = 260-360$ mm).

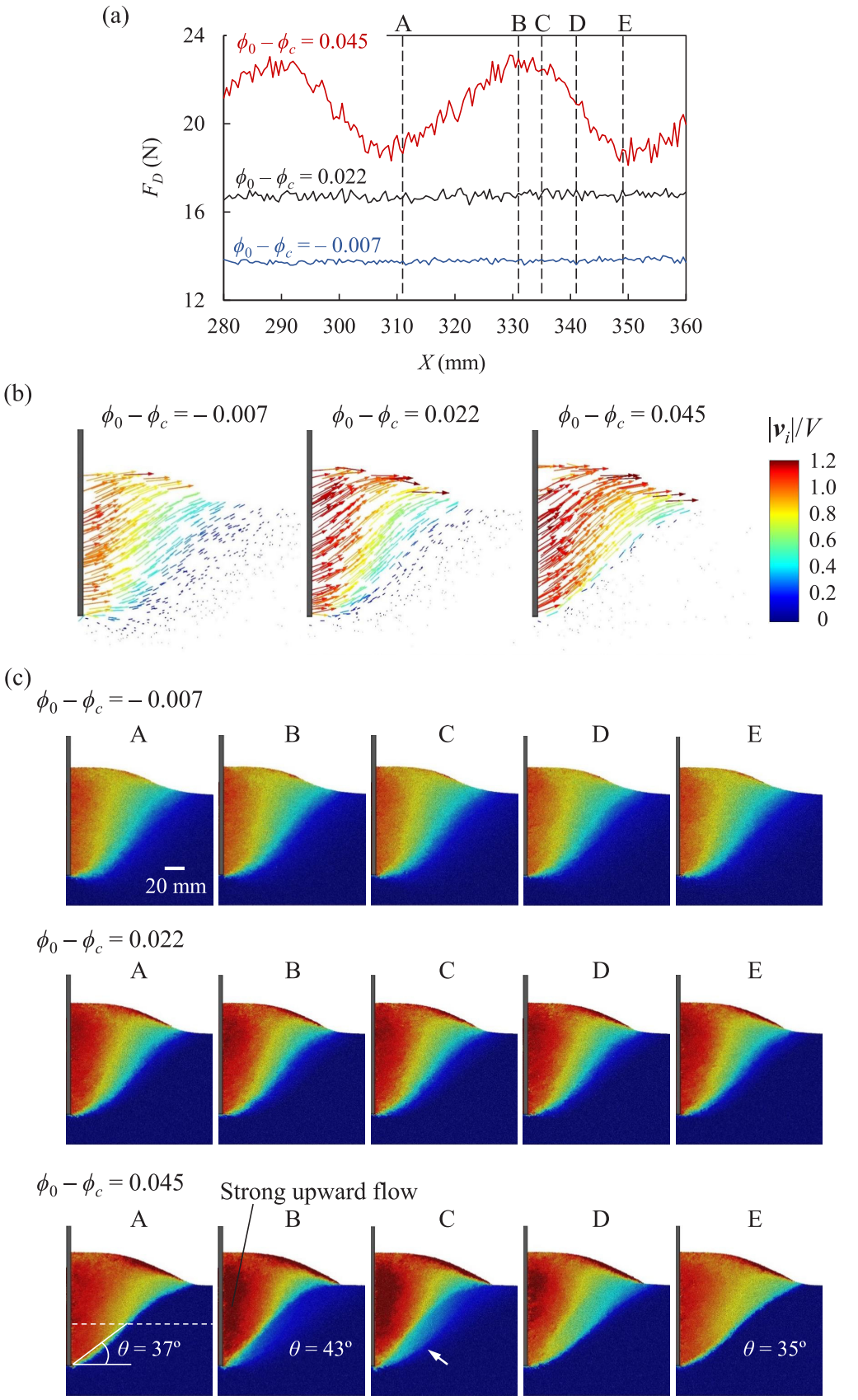

FIG. 7. Relationship between the fluctuation of drag force and the evolution of granular flow for $\phi_0 - \phi_c = -0.007$, 0.022, and 0.045. (a) Magnified figure of F_D in the plate displacement $X = 280$–360 mm in Fig. 4. (b) Velocity fields in the displacement $X = 311$ mm corresponding to point A in (a). (c) Normalized velocity $|\boldsymbol{v}_i|/V$ of the particles at five different plate displacements corresponding to points A–E in (a).

upward owing to the advance of the plate. Undisturbed materials outside this flow region are almost at rest. A boundary is formed between the disturbed flow region and the undisturbed region from the lower tip of the plate, and it reaches the free surface. For lower $\phi_0 - \phi_c$, the boundary is not clearer; i.e., the flow region is weakly confined because the loosely packed materials easily fail owing to the plate motion. For higher $\phi_0 - \phi_c$, the boundary is clearer; i.e., the flow region is strongly confined because the densely packed materials are stable.

To discuss the relationship between the fluctuation of the drag force and the evolution of the flow region, particles at five different plate displacements [points A–E in Fig. 7(a)] are shown in Fig. 7(c), where the color of the particles represents $|\boldsymbol{v}_i|/V$. For $\phi_0 - \phi_c = -0.007$ and 0.022, the velocity distribution of the particles remains unchanged in spite of the different plate locations, and the drag force has an approximately constant value [see Fig. 7(a)]. Meanwhile, for $\phi_0 - \phi_c = 0.045$, from point A to point B, the average angle of the flow boundary θ increases and the force also increases. At point B, the velocities of the particles near the plate become higher because the increased angle of the boundary induces a strong upward flow. At point C, a new boundary with a low angle nucleates (white arrow), and from point C to point E, the new boundary is fully developed and the force falls. In [13], it was reported that the dynamics of the evolution of the boundary can be captured by a friction-based wedge-flow model.

Figure 8 shows space-time plots of $|\boldsymbol{v}_i|/V$ along the centerline of the plate depth [e.g., dashed line at point A for $\phi_0 - \phi_c = 0.045$ in Fig. 7(c)]. For $\phi_0 - \phi_c = -0.007$ and 0.022, the flow region constantly moves into the undisturbed materials as the plate advances [Figs. 8(a) and 8(b)]. For $\phi_0 - \phi_c = 0.045$, the spatiotemporal evolution of the flow region is periodic; i.e., although the plate constantly moves forward, the flow boundary remains almost stationary between two successive events of the boundary formation [Fig. 8(c)]. It is also noted that materials far from the plate move incipiently before the boundary formation (i) and the materials come to rest again after the formation (ii).

E. Shear band

To identify the shear band in the materials, we compute the maximal shear strain rate from continuous velocity fields that are obtained from a spatial averaging of velocities of particles around points in the simulation space [19]. The definition of the maximal shear strain rate $\dot{\gamma}$ is the same as in the experiments [18]:

$$\dot{\gamma} = \sqrt{\left(\frac{\dot{e}_{xx} - \dot{e}_{zz}}{2}\right)^2 + \dot{e}_{xz}^2}, \tag{11}$$

where $\dot{e}_{xx}$ and $\dot{e}_{zz}$ are the normal strain rates given by

$$\dot{e}_{xx} = \frac{\partial u_x}{\partial x}, \tag{12}$$

$$\dot{e}_{zz} = \frac{\partial u_z}{\partial z}, \tag{13}$$

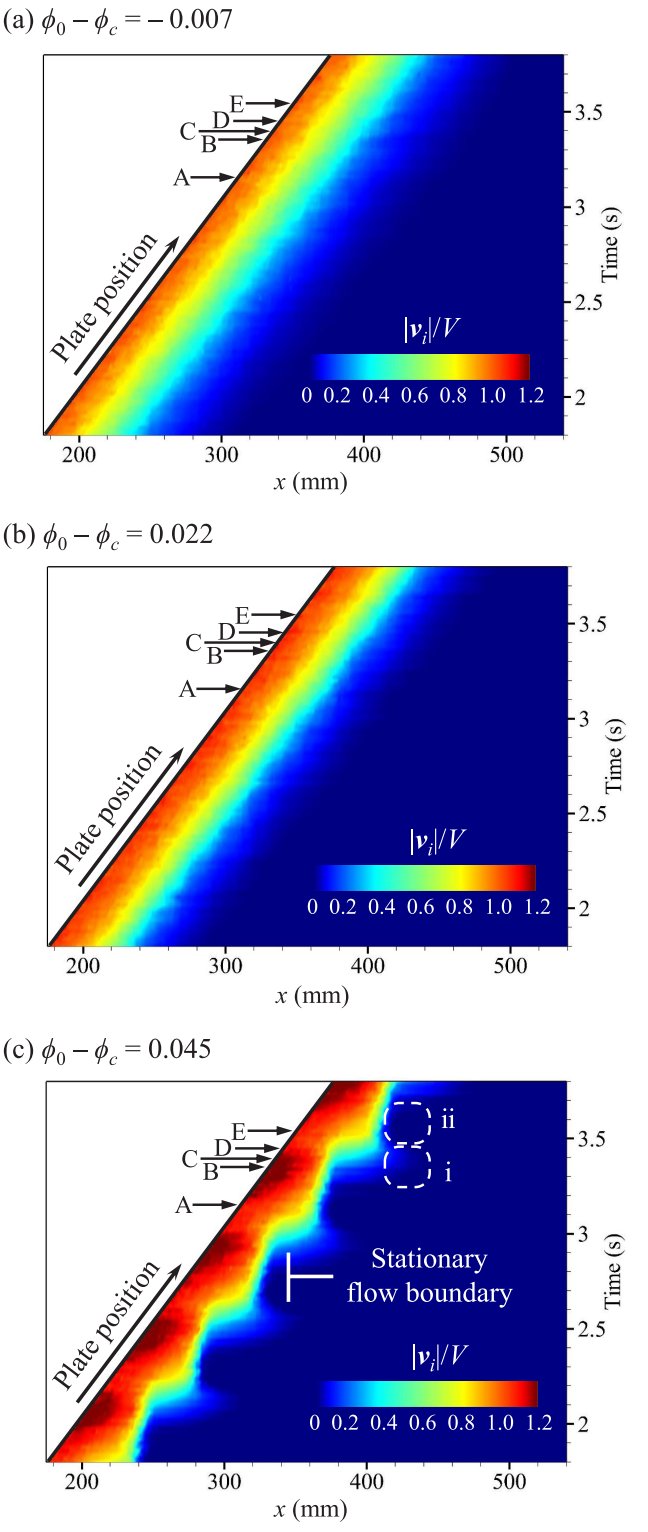

FIG. 8. Space-time plots of the normalized velocity $|\boldsymbol{v}_i|/V$ along the centerline of the plate depth for (a) $\phi_0 - \phi_c = -0.007$, (b) $\phi_0 - \phi_c = 0.022$, and (c) $\phi_0 - \phi_c = 0.045$.

and where u_x and u_z are the horizontal and vertical velocities, respectively. $\dot{e}_{xz}$ is the shear strain rate given by

$$\dot{e}_{xz} = \frac{1}{2}\left(\frac{\partial u_x}{\partial z} + \frac{\partial u_z}{\partial x}\right). \tag{14}$$

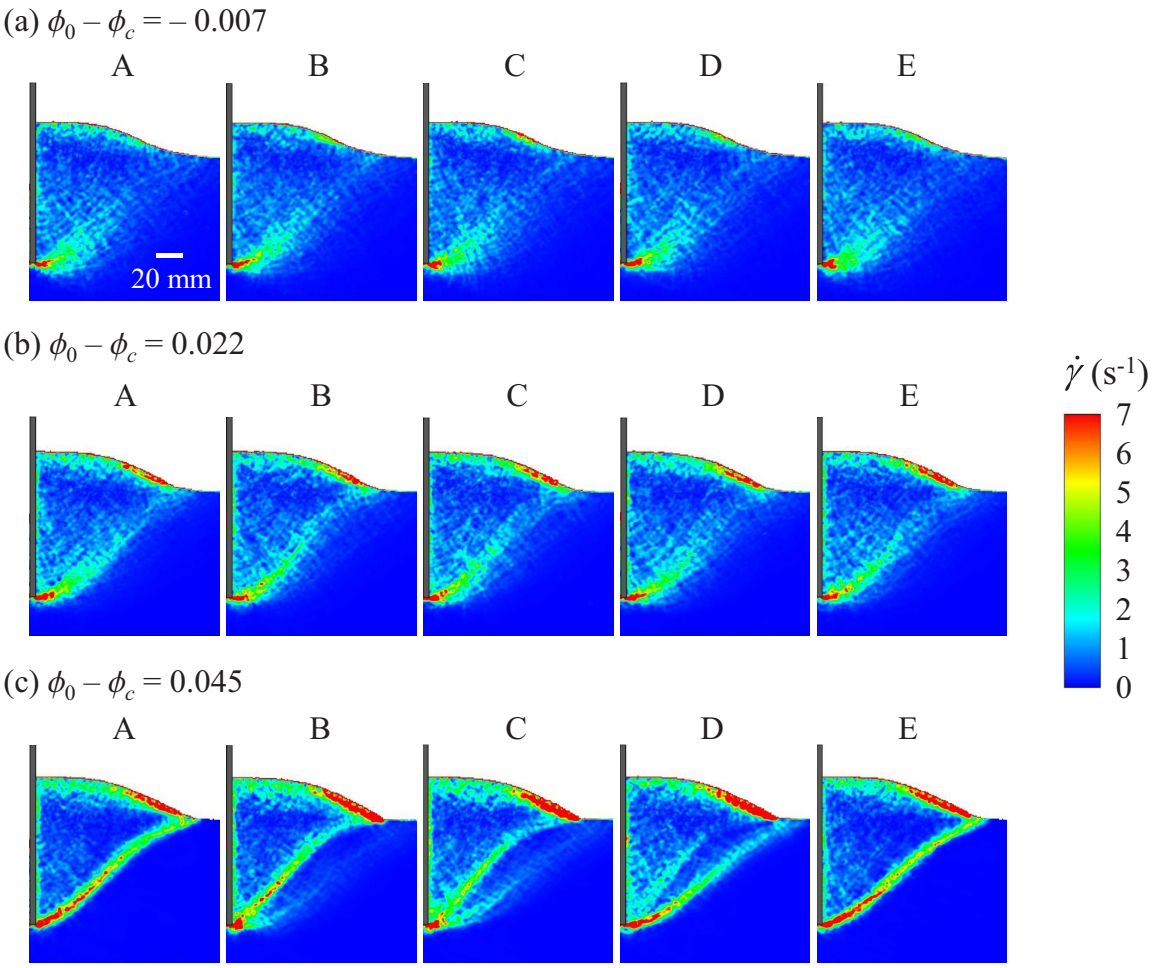

FIG. 9. Maximal shear strain fields corresponding to the granular flow in Fig. 7(c) for (a) $\phi_0 - \phi_c = -0.007$, (b) $\phi_0 - \phi_c = 0.022$, and (c) $\phi_0 - \phi_c = 0.045$.

Figure 9 shows the maximal strain rate fields that correspond to the velocity fields in Fig. 7(c). For $\phi_0 - \phi_c = -0.007$, the shear strain is distributed in the flow region, although the strain is slightly concentrated near the plate tip. The strain rate field remains unchanged in the different plate displacements as it is for the velocity distribution in Fig. 7(c). For $\phi_0 - \phi_c = 0.022$, the shear strain is slightly localized in a narrow region along the flow boundary, i.e., a vague shear band that originates at the bottom of the plate and extends upwards to the free surface. For $\phi_0 - \phi_c = 0.045$, the shear strain is strongly localized along the flow boundary, i.e., a clear shear band. It can be seen that the shear bands are created and destroyed as the plate advances. Figure 10 shows space-time plots of the maximal strain rate along the centerline of the plate depth. For $\phi_0 - \phi_c = 0.022$, the vague shear band constantly moves as the plate advances; i.e., the evolution of the shear band is not periodic. For $\phi_0 - \phi_c = 0.045$, the shear band remains almost stationary between its formation events, as we observed for the flow boundary in Fig. 8(c). The oscillation of the drag force for $\phi_0 - \phi_c = 0.045$ is attributed to the evolution of the shear band developed along the flow boundary.

F. Local volume fraction

To understand the origin of the formation of the shear band depending on ϕ_0, local compaction or dilation in the materials is investigated by calculating the local volume fraction. The local fraction at a point is computed from the total particle volume inside a sphere of radius $R = 4D_{p50}$ centered at the point [40]. To accurately calculate the local fraction, the partial volume (inside the sphere) of particles that intersect the sphere surface is considered. Figure 11 shows the distribution of the local volume fraction ϕ_{local} in the granular flow of Fig. 7(c), where the distribution in the horizontal cross section through the center of the plate depth as well as that in the vertical section are also shown (see Supplemental Material [37]). For $\phi_0 - \phi_c = -0.007$, there are no significant variations in the local volume fraction in the materials because ϕ_0 is close to ϕ_c. For higher $\phi_0 - \phi_c$, there is a considerable dilation by the plate drag. For $\phi_0 - \phi_c = 0.045$, at point A, the flow region has a much lower fraction than the undisturbed region. At point B, materials just outside the flow boundary slightly dilate (white arrow). From point C to point E, a shear band with a low volume fraction develops in the dilated materials. Finally, the dilated materials

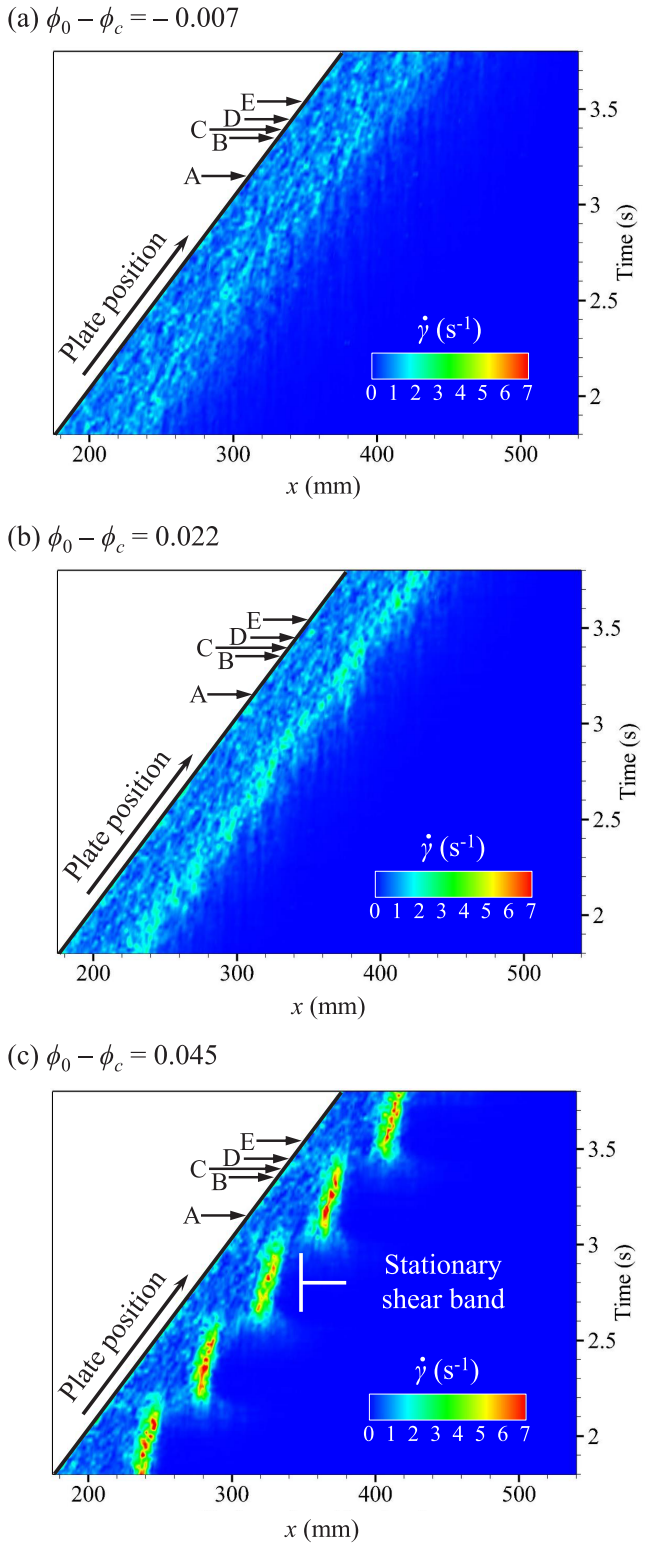

FIG. 10. Space-time plots of the maximal shear strain rate $\dot{\gamma}$ along the centerline of the plate depth for (a) $\phi_0 - \phi_c = -0.007$, (b) $\phi_0 - \phi_c = 0.022$, and (c) $\phi_0 - \phi_c = 0.045$.

between the flow region and the new band diffuse in the flow region.

To quantitatively examine the local volume fraction inside the shear band, in Fig. 12, the maximal shear strain rate $\dot{\gamma}$ and the local volume fraction ϕ_{local} along the centerline of the plate depth at point A are plotted as a function of the relative position from the plate surface $x - X$. The horizontal dashed line indicates the critical fraction ϕ_c determined in Fig. 5. For $\phi_0 - \phi_c = -0.007$, as described above, the strain is distributed in the flow region, and a shear band is not formed. For $\phi_0 - \phi_c = 0.045$, the flow region is within the range of $x - X = 0-68$ mm, in which the strain rate exceeds zero. The strain rate has a peak at $x - X = 54$ mm, i.e., the shear band. The thickness of the shear band (about 10 mm) is approximately 10 times the mean particle size ($D_{p50} = 0.8$ mm), which is in agreement with previous studies [41]. It can be seen that ϕ_{local} in the shear band ($\approx 0.580-0.590$) is slightly lower than ϕ_c (0.593).

In shear bands in granular materials, the materials self-organize a critical volume fraction ϕ_s independent of the initial volume fraction ϕ_0 [28]. Gravish *et al.* assumed that ϕ_s is equal to ϕ_c. However, the DEM result shows that these are not exactly the same, because ϕ_s and ϕ_c are determined by the dynamic and static equilibria between dilation and compaction, respectively.

Figure 13 shows space-time plots of the local change in volume fraction $\Delta\phi = \phi_{\text{local}\,(t)} - f_{\text{local}\,(t=0)}$ along the centerline of the plate depth. The positive and negative values of $\Delta\phi$ indicate the local compaction and dilation, respectively. The region far from the plate with $\Delta\phi = 0$ is the undisturbed region. For all values of ϕ_0, the materials dilate in the flow region near the plate. However, for $\phi_0 - \phi_c = -0.007$, a wide compacted front builds up ahead of the flow region. Because the compacted front advances into the weaker undisturbed region, the flow region behind the front can constantly move forward. As a result, as shown in the shear strain rate fields [Fig. 9(a)], the shear strain is not localized. For $\phi_0 - \phi_c = 0.022$ and 0.045, such a compacted front is not observed. Because the denser undisturbed region is more stable than the flow region, the flow region is strongly confined. The shear strain is localized along the flow boundary, leading to the formation of the shear band [Figs. 9(b) and 9(c)]. As shown in Figs. 10(b) and 10(c), for $\phi_0 - \phi_c = 0.022$, the evolution of the vague shear band is not periodic, and the drag force does not oscillate. For $\phi_0 - \phi_c = 0.045$, the periodic evolution of the clear shear band causes the oscillation of the drag force.

To quantitatively examine the length of the compacted front built only for $\phi_0 - \phi_c = -0.007$, in Fig. 14, the average $\Delta\phi$ along the centerline of the plate depth is plotted as a function of the relative position from the plate surface $x - X$, where the data are obtained by averaging over a plate displacement of $X = 260-360$ mm. It is observed that the compacted front with the length of 110 mm ($x - X = 70-180$ mm) builds up ahead of the flow region with 70 mm ($x - X = 0-70$ mm).

Based on this large-scale DEM simulation, it is confirmed that the spatial heterogeneous distribution of the volume fraction induced by the local dilatancy is the origin of the bifurcation of the drag force.

IV. CONCLUSIONS

Plate drag is a simple but important example of localized forcing of granular materials because it is relevant in understanding how animals, robots, and tools interact with

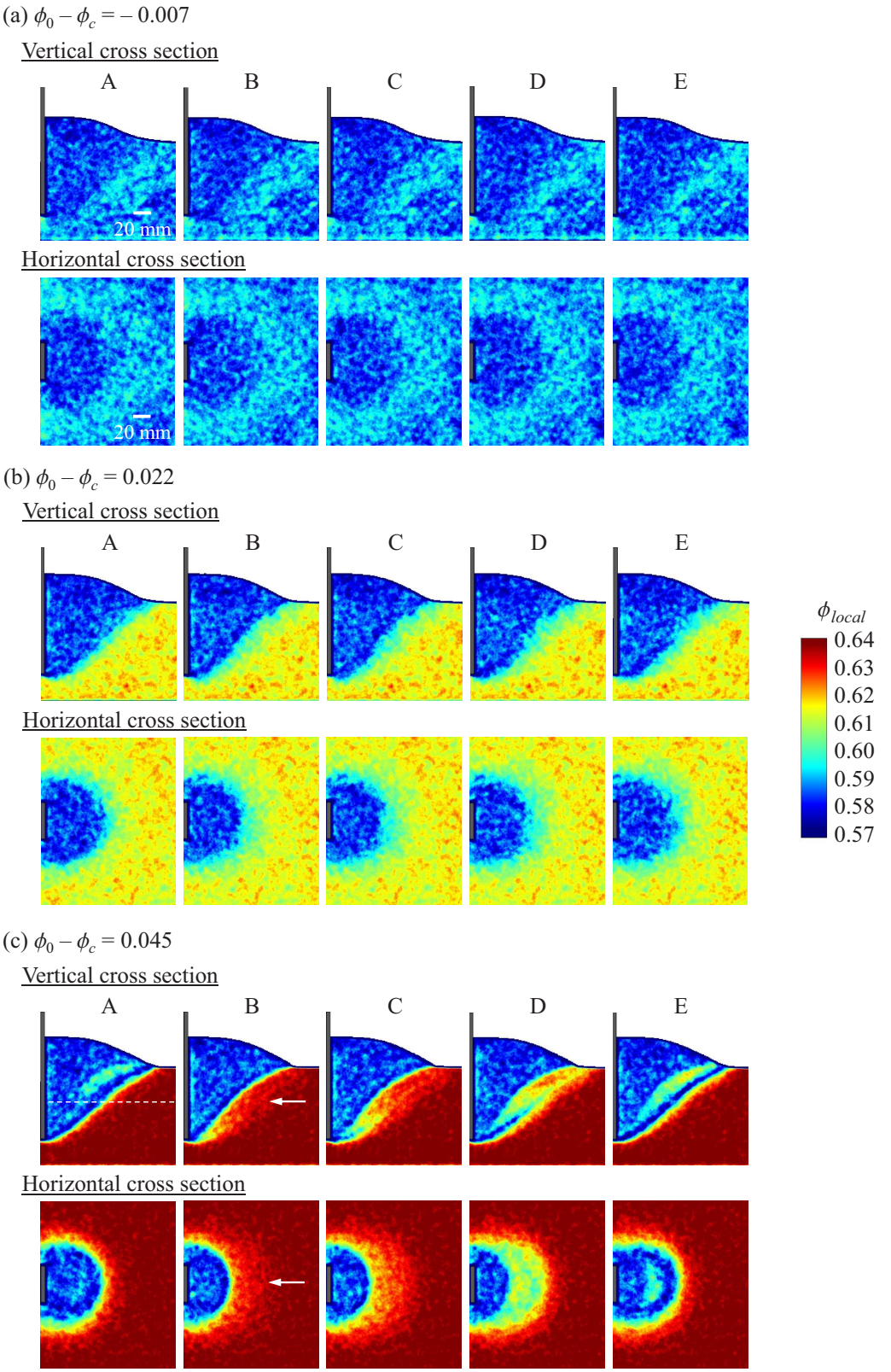

FIG. 11. Distribution of local volume fraction ϕ_{local} corresponding to the granular flow in Fig. 7(c) for (a) $\phi_0 - \phi_c = -0.007$, (b) $\phi_0 - \phi_c = 0.022$, and (c) $\phi_0 - \phi_c = 0.045$, where the distributions in the horizontal cross section through the center of the plate depth as well as that in the vertical section are shown.

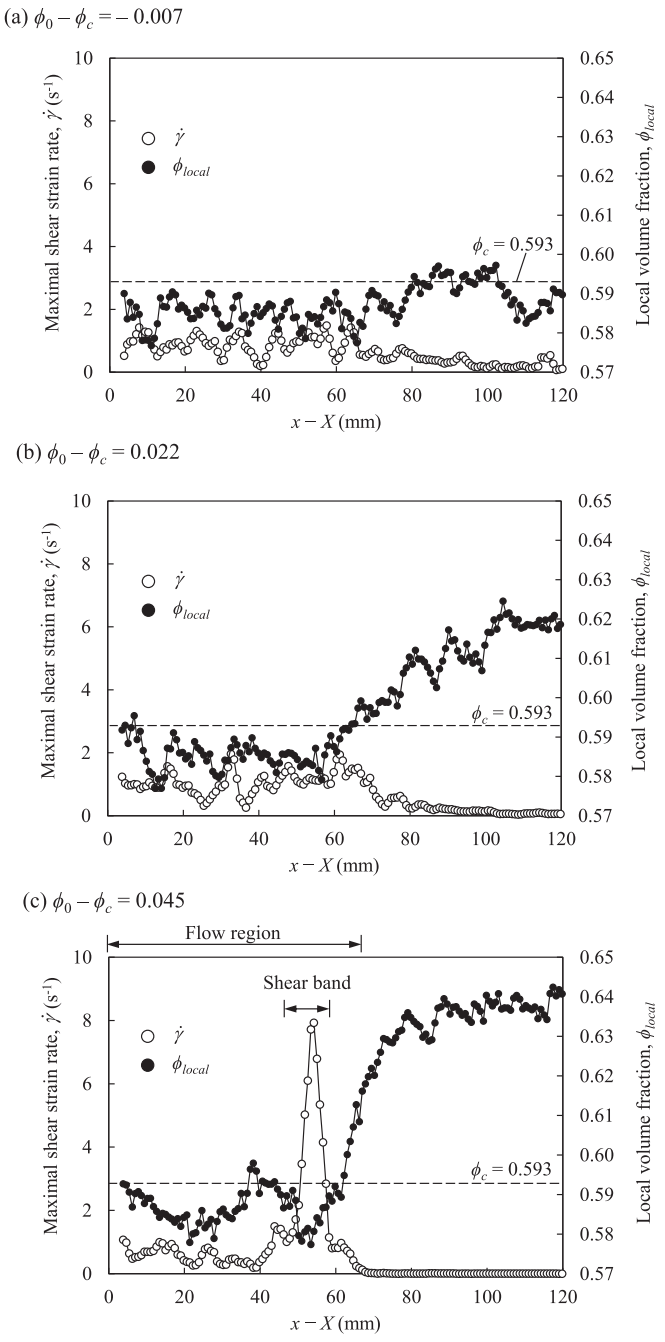

FIG. 12. Maximal shear strain rate $\dot{\gamma}$ and local volume fraction ϕ_{local} along the centerline of the plate depth as a function of the relative position from the plate surface $x - X$ at point A for (a) $\phi_0 - \phi_c = -0.007$, (b) $\phi_0 - \phi_c = 0.022$, and (c) $\phi_0 - \phi_c = 0.045$. The horizontal dashed line indicates the critical fraction ϕ_c determined in Fig. 5.

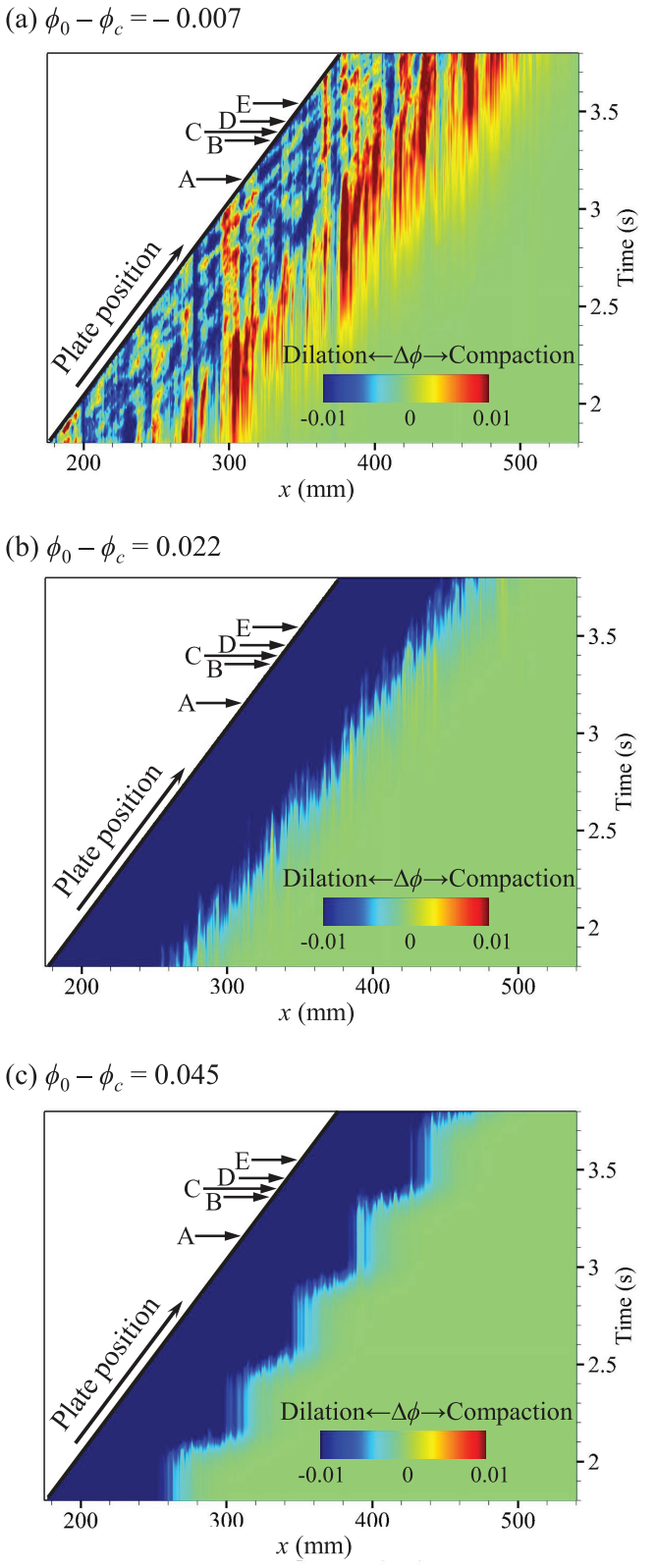

FIG. 13. Space-time plots of the local change in volume fraction $\Delta\phi = \phi_{\text{local}\,(t)} - \phi_{\text{local}\,(t=0)}$ along the centerline of the plate depth for (a) $\phi_0 - \phi_c = -0.007$, (b) $\phi_0 - \phi_c = 0.022$, and (c) $\phi_0 - \phi_c = 0.045$. The positive and negative values of $\Delta\phi$ indicate the local compaction and dilation, respectively.

soil during their locomotion. In this study, we numerically investigated the response of granular materials to plate drag using a large-scale DEM simulation. The effect of the initial volume fraction ϕ_0 of the materials on the drag force acting on the plate has been examined. The plate size, depth, and speed were nearly identical to those in previous experiments performed by Gravish *et al.* [13,18] but the particles were about three times larger than those in their experiments.

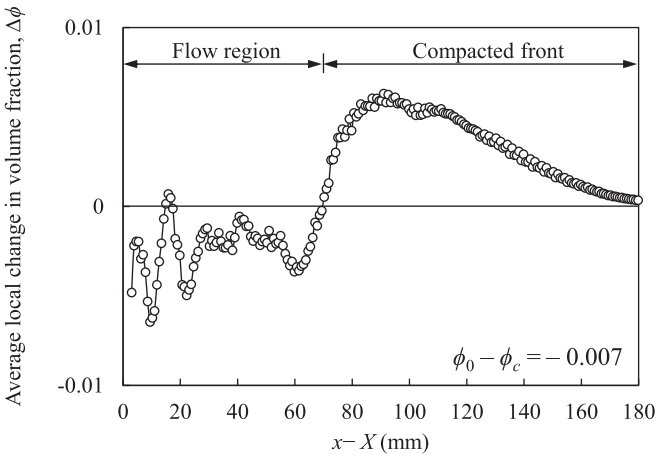

FIG. 14. Local change in volume fraction $\Delta\phi$ along the centerline of the plate depth as a function of the relative position from the plate surface $x - X$ for $\phi_0 - \phi_c = -0.007$, where the data are obtained by averaging over a plate displacement $X = 260-360$ mm.

Following up the experiments, we confirmed the following points numerically:

(1) The average drag force over a steady state increases approximately linearly with ϕ_0.

(2) A volume-fraction-dependent bifurcation occurs in the force; for low ϕ_0, the force reaches an approximately constant value as the plate advances, while for high ϕ_0, the force oscillates with a large amplitude. The force oscillation is attributed to the periodic evolution of a shear band formed in the bed.

(3) The formation of the shear band is divided into two regimes above and below ϕ_c (ϕ_c is the critical fraction corresponding to the onset of dilatancy).

Additionally, the large-scale DEM simulation allows us to perform a grain level microscopic investigation and the following findings are revealed:

(1) Due to an increased coordination number of the initial granular bed, the average force increases with ϕ_0.

(2) The evolution of the shear band formed only for $\phi_0 > \phi_c$ is divided into two regimes; i.e., for $\phi_c < \phi_0 < \phi_c + \alpha$, the evolution of the shear band is not periodic and for $\phi_0 > \phi_c + \alpha$, the evolution is periodic (in this study, $\alpha = 0.03$). As a result, the force oscillation occurs for $\phi_0 > \phi_c + \alpha$. From the experiments and our previous DEM study [34], it may be concluded that α depends on the particle size and decreases to zero as the particle size reduces.

(3) The formation of the shear band above ϕ_c is explained by the analysis of the local volume fraction as follows. Independent of ϕ_0, materials dilate in a flow region that forms in front of the plate. For $\phi_0 < \phi_c$, a compacted front builds up ahead of the flow region. Because the compacted front advances into the weaker undisturbed region, the flow region behind the front can constantly advance. However, for $\phi_0 > \phi_c$, such a compacted front is not observed. Because the denser undisturbed region is more stable than the flow region, the flow region is strongly confined. Consequently, the shear strain is localized along the flow boundary and the shear band develops.

(4) Although in the previous study, it was assumed that the local volume fraction ϕ_s in a fully developed shear band is equal to ϕ_c, the DEM results show that ϕ_s is slightly lower than ϕ_c, because ϕ_s and ϕ_c are determined by the dynamic and static equilibria between dilation and compaction, respectively.

As shown in this study, localized forcing induces a spatially heterogeneous distribution of volume fraction in granular materials. Although many studies on localized forcing have been conducted, there have been few reports detailing such a distribution. One of the few reports is the experimental study by Royer *et al.*, which examined the change in the local volume fraction during the impact of a solid sphere into a granular bed using high-speed x-ray radiography [42]. The analysis of the local dilatancy in another configuration of localized forcing using large-scale simulations as well as advanced experimental techniques may also provide a better understanding of the origin of forces experienced by objects moving in granular materials.

ACKNOWLEDGMENTS

M.K., T.T., and T.T. acknowledge Komatsu Ltd. for their financial support. M.K. also acknowledges the Hosokawa Powder Technology Foundation. A part of this research used computational resources of HPCI system provided by the Academic Center for Computing and Media Studies, Kyoto University through the HPCI System Research Project (Project ID: hp160163).

[1] H. M. Jaeger and S. R. Nagel, Science **255**, 1523 (1992).
[2] H. M. Jaeger, S. R. Nagel, and R. P. Behringer, Rev. Mod. Phys. **68**, 1259 (1996).
[3] H. M. Jaeger, S. R. Nagel, and R. P. Behringer, Phys. Today **49**(4), 32 (1996).
[4] H. Katsuragi and D. J. Durian, Nat. Phys. **3**, 420 (2007).
[5] D. I. Goldman and P. Umbanhowar, Phys. Rev. E **77**, 021308 (2008).
[6] P. Umbanhowar and D. I. Goldman, Phys. Rev. E **82**, 010301(R) (2010).
[7] J. J. S. Jerome, N. Vandenberghe, and Y. Forterre, Phys. Rev. Lett. **117**, 098003 (2016).
[8] M. Schroter, S. Nagle, C. Radin, and H. L. Swinney, Europhys. Lett. **78**, 44004 (2007).
[9] E. Hamm, F. Tapia, and F. Melo, Phys. Rev. E **84**, 041304 (2011).
[10] F. Tapia, D. Espindola, E. Hamm, and F. Melo, Phys. Rev. E **87**, 014201 (2013).
[11] M. B. Stone, R. Barry, D. P. Bernstein, M. D. Pelc, Y. K. Tsui, and P. Schiffer, Phys. Rev. E **70**, 041301 (2004).
[12] I. Albert, J. G. Sample, A. J. Morss, S. Rajagopalan, A.-L. Barabási, and P. Schiffer, Phys. Rev. E **64**, 061303 (2001).
[13] N. Gravish, P. B. Umbanhowar, and D. I. Goldman, Phys. Rev. Lett. **105**, 128301 (2010).

[14] Y. Ding, N. Gravish, and D. I. Goldman, Phys. Rev. Lett. **106**, 028001 (2011).
[15] B. Percier, S. Manneville, J. N. McElwaine, S. W. Morris, and N. Taberlet, Phys. Rev. E **84**, 051302 (2011).
[16] F. Q. Potiguar and Y. Ding, Phys. Rev. E **88**, 012204 (2013).
[17] F. Guillard, Y. Forterre, and O. Pouliquen, Phys. Rev. Lett. **110**, 138303 (2013).
[18] N. Gravish, P. B. Umbanhowar, and D. I. Goldman, Phys. Rev. E **89**, 042202 (2014).
[19] F. Guillard, Y. Forterre, and O. Pouliquen, Phys. Fluids **26**, 043301 (2014).
[20] F. Guillard, Y. Forterre, and O. Pouliquen, Phys. Rev. E **91**, 022201 (2015).
[21] T. Tsuji, Y. Nakagawa, N. Matsumoto, Y. Kadono, T. Takayama, and T. Tanaka, J. Terramech. **49**, 37 (2012).
[22] C. Li, T. Zhang, and D. I. Goldman, Science **339**, 1408 (2013).
[23] T. Zhang and D. I. Goldman, Phys. Fluids **26**, 101308 (2014).
[24] J. Aguilar and D. I. Goldman, Nat. Phys. **12**, 278 (2016).
[25] B. Andreotti, Y. Forterre, and O. Pouliquen, *Granular Media: Between Fluid and Solid* (Cambridge University Press, Cambridge, 2013).
[26] C. Thornton, Geotechnique **50**, 43 (2000).
[27] L. Rothenburg and N. P. Kruyt, Int. J. Solids Struct. **41**, 5763 (2004).
[28] S. Fazekas, J. Torok, and J Kertesz, Phys. Rev. E **75**, 011302 (2007).
[29] A. Daerr and S. Douady, Europhys. Lett. **47**, 324 (1999).
[30] M. Pailha, M. Nicolas, and O. Pouliquen, Phys. Fluids **20**, 111701 (2008).
[31] F. Bonnet, T. Richard, and P. Philippe, Granular Matter **12**, 317 (2010).
[32] N. Gravish and D. I. Goldman, Phys. Rev. E **90**, 032202 (2014).
[33] D. M. Wood, *Geotechnical Modelling* (Spon Press, London, 2004).
[34] M. Kobayakawa, S. Miyai, T. Tsuji, and T. Tanaka, in *Proceedings of the 7th International Conference on Discrete Element Methods*, edited by X. Li, Y. Feng, and G. Mustoe (Springer, Berlin, 2016), pp. 1201–1208.
[35] P. A. Cundall and O. D. L. Strack, Geotechnique **29**, 47 (1979).
[36] K. Iwashita and M. Oda, J. Eng. Mech. **124**, 285 (1998).
[37] See Supplemental Material at http://link.aps.org/supplemental/10.1103/PhysRevE.98.052907 for videos from DEM simulation.
[38] Y. Tsuji, T. Kawaguchi, and T. Tanaka, Powder Technol. **77**, 79 (1993).
[39] T. Poschel and T. Schwager, *Computational Granular Dynamics: Models and Algorithms* (Springer, Berlin, 2005).
[40] M. Suzuki and T. Oshima, Powder Technol. **43**, 147 (1985).
[41] *Mechanics of Granular Materials*, edited by M. Oda and K. Iwashita (A. A. Balkema, Rotterdam, 1999).
[42] J. R. Royer, B. Conyers, E. I. Corwin, P. J. Eng, and H. M. Jaeger, Europhys. Lett. **93**, 28008 (2011).